PNAS
www.pnas.org

Supplementary Information for

Structure of the *EmrE* Multidrug Transporter and Its Use for Inhibitor Peptide Design

Victor Ovchinnikov, Tracy A. Stone, Charles M. Deber and Martin Karplus

E-mail: ovchinnv@georgetown.edu (VO), deber@sickkids.ca (CMD), marci@tammy.harvard.edu (MK)

This PDF file includes:

www.pnas.org/cgi/doi/10.1073/pnas.1802177115

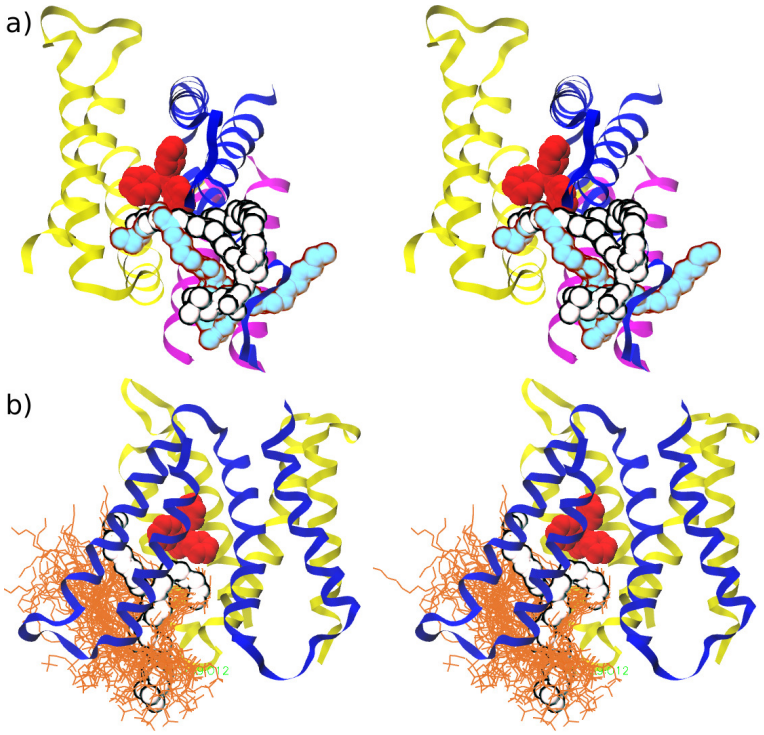

Fig. S1. Lipid penetration into the active site (wall-eyed stereo). a) *EmrE* embedded in DMPC. Cyan spheres show the penetrating lipid molecule in the original simulation; white spheres show a different lipid molecule that penetrates the active site in the reequilibration simulation after the original lipid is removed. The closed side of *EmrE* is at the top and into the page. b) *EmrE* embedded in POPC:POPG (3:1) bilayer. White spheres highlight one particular conformation of a penetrating POPC lipid molecule; orange lines illustrate the conformational ensemble of the same molecule spanning 500ns in 5ns time intervals. TPP is shown in red to indicate the binding site. For clarity, only one conformation of *EmrE* with TPP is shown.

Lipid penetration into the *EmrE* active site. In Fig. 1d of the main text, the tail of one particular DMPC lipid molecule was shown to penetrate into the *EmrE* binding site. To investigate whether the lipid penetration into the binding site was a reproducible event, we performed an additional 0.65μs MD simulation in which the lipid molecule was deleted, and the simulation box reequilibrated for 65ns. For the first 7.5ns of equilibration, harmonic positional constraints were applied to the protein with a force constant of 0.5 kcal/mol. After this time, and until 15ns, the harmonic positional restraint was applied only to the phosphorous of TPP. To prevent water from entering the void created by the deleted lipid molecule, weak forces were applied to the water molecules near the membrane in the membrane-normal (z-) direction for the first 15ns of equilibration. During this stage, a barostat was used. The remainder of equilibration was performed in the NVT ensemble without any restraints.

To investigate whether the observed lipid penetration is dependent on the lipid composition, we transferred the *EmrE* dimer equilbrated in DMPC into a POPC:POPG (3:1) membrane patch, reequilibrated the simulation structure, and performed a 0.7μs MD simulation. The equilibration was performed as described for the DMPC bilayer in SI Methods (Sec.). In both MD simulations, a lipid molecule penetrated the binding site in a similar location (Fig. S1), suggesting that it contributes to stabilize the *EmrE* dimer structure.

We note that the final active-site conformation of TPP-bound *EmrE* in the POPC/POPG lipid (Fig. S2) is slightly different from that of *EmrE* in DMPC (Fig. 2). The main difference is that in POPC/POPG TPP is buried slightly deeper in the *EmrE* active site (Fig. S2), which puts it into closer proximity with the F44 residues, and farther from E14[2]. This shift in TPP position occured spontaneously in the MD simulation (which was initiated from the structure of TPP-bound *EmrE* equilibrated in DMPC). It further underscores the role of the lipid environment in modulating membrane protein structure.

Water-mediated E14[1]-TPP interaction. Examination of the MD trajectory of the *EmrE*-TPP complex revealed that a water molecule was present between the phosphorous of TPP and the carboxyl of E14[1] (Fig. 2a) in most of the simulation frames.

To characterize this water-mediated interaction quantitatively, we first found all unique water molecules that were within 4.5Å of TPP and 4Å of both E14 carboxyls. This analysis yielded 232 waters in a 1μs trajectory. These water molecules were able to exchange with the water resevoir *via* the open side of *EmrE*. Next, we subsampled this set of waters to contain only the waters interacting with TPP and E14[1], or only the waters interacting with TPP and E14[2]. In Fig. S3, we plot the minimal sum of the distances between any water molecule and the phosphorous atom of TPP, and that between the same water molecule and the carboxyls of E14[i], where i is 1 in panel (a) and 2 in panel (b). When the identity of the closest water molecule changes, the color of the plot is changed. The figure shows that a persistent mediating water molecule is present between TPP and E14[1], but not between TPP and E14[2], although water molecules occasionally approach the latter pair. The average occupancy for a water molecule in (a) is about

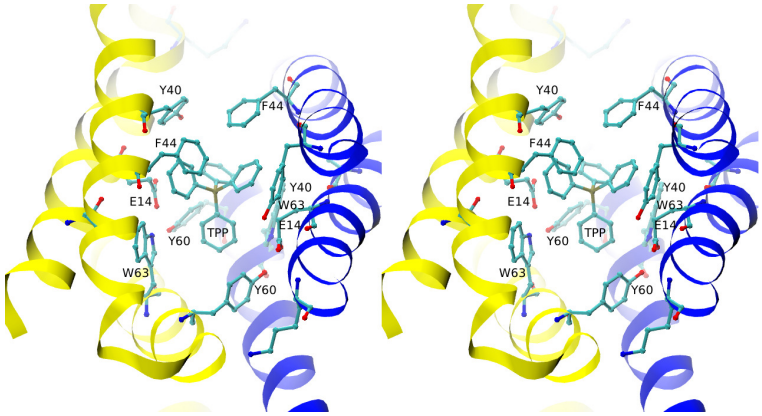

Fig. S2. Active site of the *EmrE* dimer with ligand TPP equilibrated in a POPC:POPG (3:1) lipid bilayer.

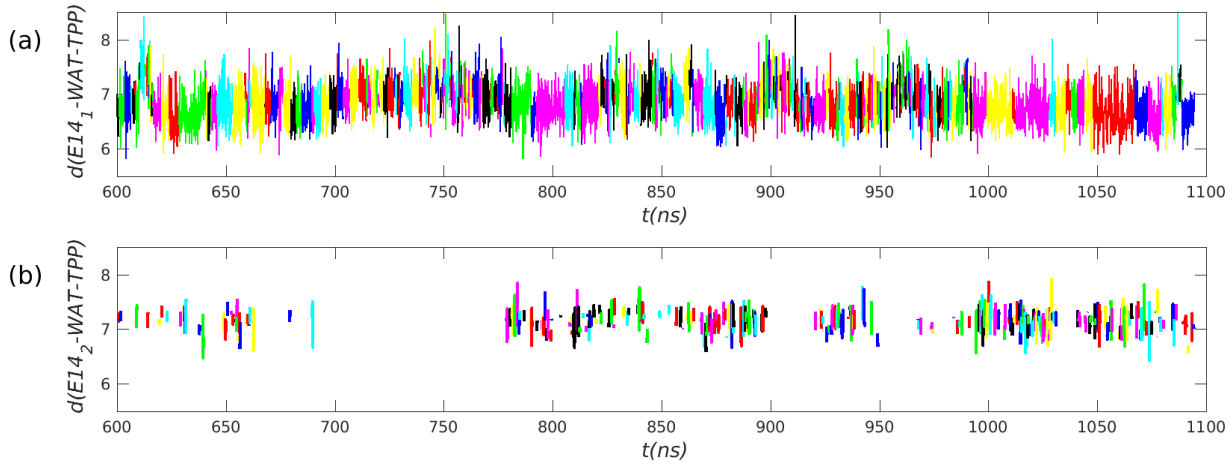

Fig. S3. Minimal sum of the distances between any water molecule and the phosphorous atom of TPP, and that between the same water molecule and the carboxyls of E14[1] (a), and E14[2] (b) When the identity of the closest water molecule changes, the color of the plot is changed.

1ns, although, occasionally, the same water molecule remains the mediator for ∼20ns (see the distace trace at t=∼1050ns in Fig. S3a). Considering only those water molecules at the center of the interaction $E14$-O_{wat}-TPP with the interaction angle above 90^o, we calculated that such an interaction was present 77% of the time. A similar analysis done on the MD trajectory with *EmrE* bound to ethidium revealed only transient interactions, *i.e.* the results were similar to Fig. S3b rather than Fig. S3a.

Interaction energy analysis between ligands and active site residues.. To examine the possible origins of the lower binding affinity of *EmrE* for ethidium *vs.* TPP, we computed interaction energies between seven residues in the active site whose side chains were found to be in the closest proximity to the ligand. These residues were E14, T18, Y40, F44, L47, Y60 and W63; their positions are shown in Fig. 2, except for T18 and L47, which were found to have the weakest interactions with the ligands (see Fig. S4 below), and were omitted. Electrostatic and van der Waals (vdW) interactions were computed between all ligand atoms and all atoms of a given residue, usign a cutoff of 12Å for both electrostatic and vdW interactions, and the results averaged over the corresponding trajectories. Figure S4a shows the electrostatic and vdW interaction energies computed separately for each monomer, and Fig. S4b shows the total interaction energy for each residue type. For both ligands, the dominant electrostatic and vdW interactions involved residues E14 and W63, respectively; TPP had stronger electrostatic interactions with the E14s than did ethidium, but weaker interactions with the W63s than did ethidium. However, increased vdW interactions with ethidium were not sufficient to offset the decreased electrostatic interactions, relative to TPP, resulting in more favorable interaction energies between *EmrE* and TPP. The analysis underscores that both electrostatic and vdW interactions are important to binding, with the corresponding contributions dependent on the ligand, and the particular importance of residues E14 and W63.

EmrE **E14D mutant.** An additional illustration of the structural plasticity of the *EmrE* binding site comes from MD simulations of the E14D double mutant The mutant protein has been shown to bind TPP, but the proton-coupled efflux is reduced and its pH dependence is shifted toward lower values.(1, 2) The E14D mutation was performed *in silico* using CHARMM(3) by deleting the carboxyl groups from E14 and rebuilding the residues as aspartates, followed by energy minimization. A 0.3μs MD simulation was performed starting from the resulting structure. Because the simulation structure remained very stable, with a backbone-atom RMSD to the initial structure of about 1.2Å, a longer simulation was not deemed necessary.

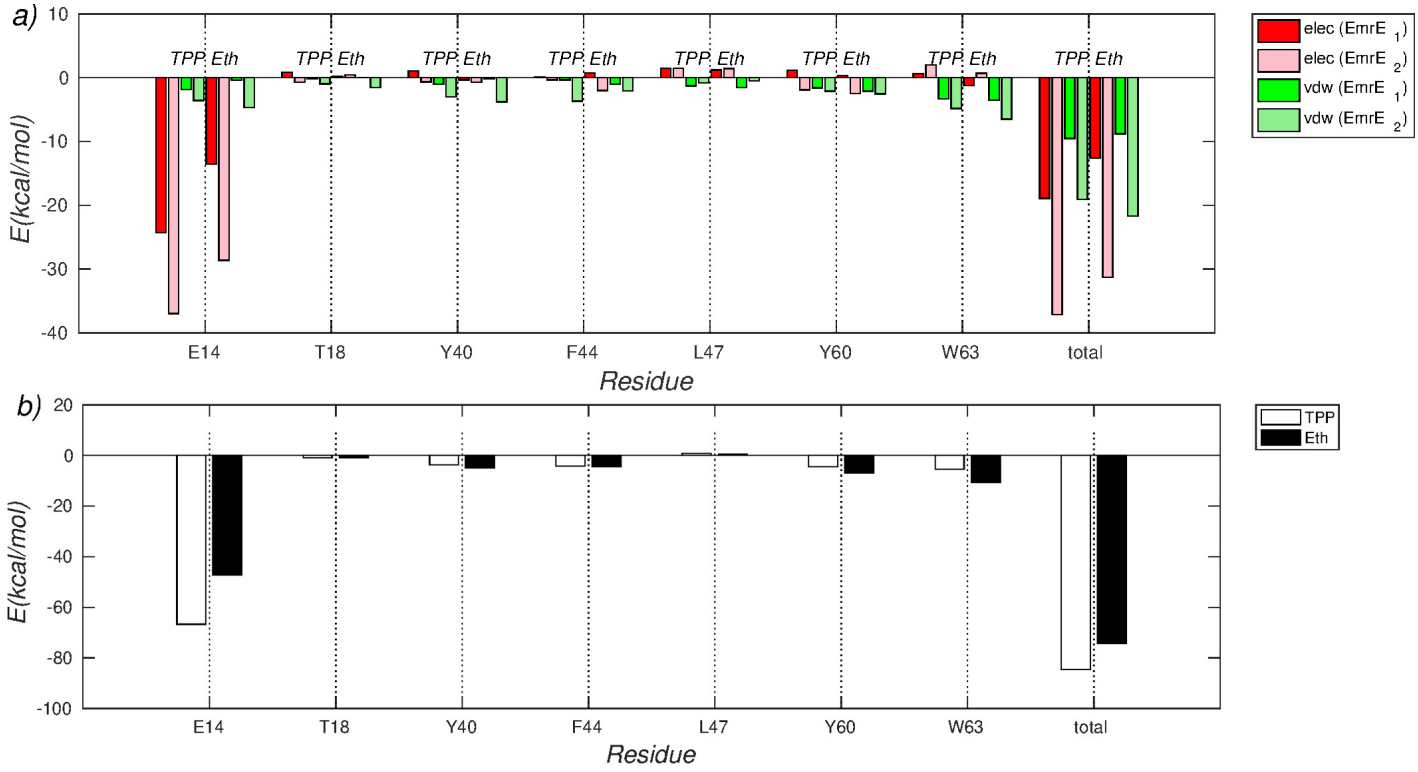

Fig. S4. Interaction energies between ligands and binding-site residues. The chosen residues have the closest proximity to the ligand binding site. In (a), the interaction energy is decomposed into electrostatic and van der Waals contributions, as well as into the individual contributions of the *EmrE* monomers. In (b), the total interaction energy is shown for each residue, and for each ligand.

The main difference between the active site structures of the E14D mutant and the wild type dimer is in the position of D14[2]. Because the side chain is shortened by 1 C-C bond (∼1.5Å) the carboxyl group does not protrude as far toward to the TPP phosphorous as in the wild type dimer (see Fig. 2a). The position of the shorter D14[2] side chain is now stabilized by a hydrogen bond to a rotated Y40[2] side chain on the same monomer. The structure of the active site on the side of monomer 1 is qualitatively similar to that in the WT dimer, the main difference being that Y40[1] approaches more closely to the shorter D14[1], with d(D14OD, Y40OH)∼ 3Å, compared to 5Å in the WT dimer.

Interpretation of mutagenesis data. The equilibrated structure provides structural explanations of mutagenesis data available for residues other than those in direct contact with substrates. Following Lloris-Garcerá et al. (5), in Fig. S7 we show the alignment of 15 representative sequences from the multidrug resistance family PF00893.(4) Figure S8 shows the positions of residues discussed below. The conservation of residues A10(15/15) and G67(14/15) can be explained on the basis of the position of W63 in the present structure (the numbers in parentheses indicate conservation within the 15-sequence set). The bulky side chain of W63 does not point directly into the active site interior, but instead toward H1, which allows it to interact with E14, as described above. Its side chain is sufficiently large that it would clash with that of a mutated G67. If either A10 or G67 were substituted for an amino acid with a larger side chain, steric hindrance would likely force W63 to change conformation, *e.g.* to protrude into the active site, which would alter the the active site geometry sufficiently to abolish transport activity, or to alter ligand binding. This explanation is consistent with the fact that the mutation A10G, in which the side chain A10 is removed completely, results in a dimer with TPP affinity similar to WT, although the mutation impairs proton-driven drug transport.(2) An additional explanation for the conservation of G67(14/15) is that it provides a hinge for the kinking of H3, which brings the C-terminal portion of H3 in closer proximity to H1 on the same monomer and to H3 on the opposite monomer (see Fig. S8), stabilizing the dimer. Kinking of H3 was also detected by Amadi et al. (6) on the basis of EPR studies, and could facilitate the interconversion between inward and outward-open conformations of *EmrE*,(7) possibly by stabilizing an intermediate conformation.

Similarly, adding a side chain to G17(7/15; G17A 4/15) would lead to steric clashes with the side chain and the ring of Y40[1], which is involved in interactions with E14, as described above. If the ring of Y40[1] were to protrude directly into the binding site, it would interfere sterically with the binding of a ligand. Mutagenesis experiments found that the G17C mutant does not bind substrate.(2)

Steric reasons could also explain the conservation of G65(14/15). If the glycine had a side chain, it would protrude directly into the interface between H3 and H4 helices, which could increase the distance between these helices. A recent mutagenesis study examined the effect of mutations in the loop 81-84 that links H3 and H4, and found that lengthening of this loop leads to a loss of resistance to ethidium.(8) The interpretation was that longer loops allowed a decoupling of H4 from H3, which could also occur upon G65 mutations.

Lloris-Garcerá et al. (5) found that the mutation T36W effectively inactivates *EmrE*. This finding seemed puzzling in view of the C_α

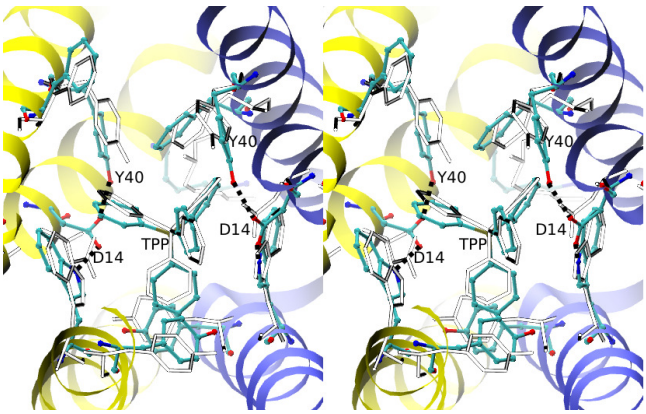

Fig. S5. Stereo view of the active site of the E14D double mutant with bound TPP. The active site residue conformations after the E14D $in\ silico$ mutation but prior to equilibration are shown in black-and-white. The D14/W63 and D14/Y40 hydrogen bonds formed after equilibration are indicated in dotted lines.

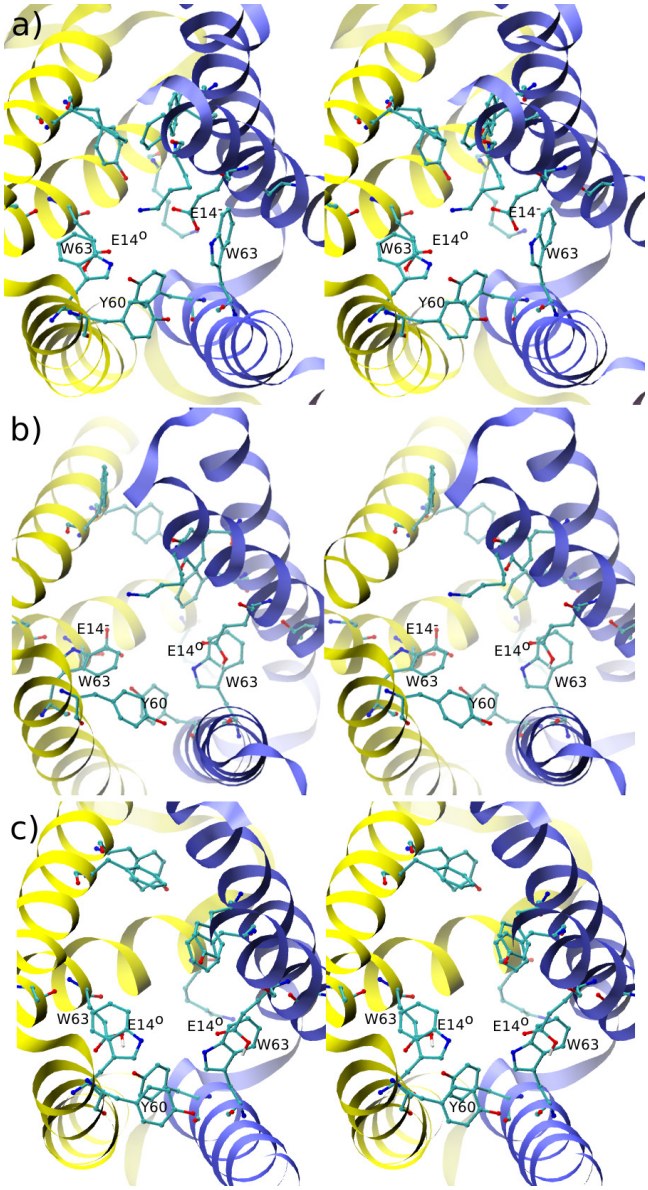

Fig. S6. Active site of the ligand-free $EmrE$ **dimer protonated on E14.** Panels a), b) and c) correspond to the equilibrated structures with E14 protonated on monomer 1, 2, and on both monomers, respectively. Protonated and deprotonated E14s are indicated with superscripts ^{0} and $^-$, respectively, which reflect the charge on the carboxyl groups.

```
                                        10        20             30        40        50        60        70        80        90
EMRE_ECOLI/2-94 (100%) NPYI---YLGGAILAEVIGTTLMKF-------SEGFTRLWPSVGIII---CYCASFWLLAQTLAY-IPTGIAYAIWSGVGIVLISLLSWGFFGQRLDLPAIIGMMLI
YVDR_BACSU/1-93  (30%) MAWF---LLVIAGIEEIIAAIAMKY-------IDGTRKKWPIIVMTV---GFGLSFYCLSQAMIV-LPAGVAYAVWTGIGSIGVSAVGLIWFKERFQLSQVISLCLI
B4EWY3_PROMH/1-93(32%) MSWI---ILFVAGLLEIVWAVGLKY-------THGFTRLTPSIITIS---AMIVSMGMLSYAMKG-LPAGTAYAIWTGIGAVGTAIFGIIVFGESANIYRLLSLAMI
SUGE_ECOLI/1-93  (33%) MSWI---ILVIAGLLEVVWAVGLKY-------THGFSRLTPSVITVT---AMIVSMALLAWAMKS-LPVGTAYAVWTGIGAVGAAITGIVLLGESANPMRLASLALI
YKKD_BACSU/2-94  (29%) LHWI---SLLCAGCLEMAGVALMNQ-------YAKEKSVKWVLLIIV---GFAASFSLLSYAMET-TPMGTAYAVWTGIGTAGGALIGILFYKEQKDAKRIFFIALI
YVDS_BACSU/1-89  (24%) MNWV---LVFIAGLLEVVWASSLK---------HADSLLDWIIIFIL----IAVSFILLIRSYQK-IPMAAAYTVFVGIGTVGTYLTGIVL-GESFSAAQMFFLALL
YKKC_BACSU/1-90  (22%) MKWG---LVVLAAVFEVVWVIGLK---------HADSALTWSGTAI----GIIFSFYLLMKATHS-LPVGTVYAVFTGLGTAGTVLSEIVLFHEPVGWPKLLLIGVL
MDTJ_SHIDS/4-94  (32%) -YWI---LLGLAIATEITGTLSMKW-------ASVSEGNGGFILMLV---MISLSYIFLSFAVKK-IALGVAYALWEGIGILFITLFSVLLFDESLSLMKIAGLTT-
YVAE_BACSU/1-93  (43%) MNWV---FLCLAILFEVAGTVSMKL-------SSGFTKLIPSLLLIF---FYGGSLFFLTLTLKS-IDVSVAYAVWSGMGIVLITVVGFLFFQEHVSVMKVISIGLI
EBRA_BACSU/3-95  (38%) IGYI---FLTIAICSESIGAAMLKV-------SDGFKKWKPSALVVI---GYSLAFYMLSLTLNH-IPLSLSYATWSGAGTVLTTVIGVKWFKEDLNAKGLIGILLL
MDTI_ECOLI/4-99  (33%) FEWVHAAWLALAIVLEIVANVFLKF-------SDGFRRKIFGLLSLA---AVLAAFSALSQAVKG-IDLSVAYALWGGFGIAATLAAGWILFGQRLNRKGWIGLVLL
EBRB_BACSU/2-94  (39%) RGLL---YLALAIVSEVFGSTMLKL-------SEGFTQAWPIAGVIV---GFLSAFTFLSFSLKT-IDLSSAYATWSGVGTALTAIVGFLLFGETISLKGVFGLTLV
E6W493_DESIS/3-94(47%) -GWL---FLVIAIVGEVIATSALKS-------SEGFTKLAPSAVVII---GYGIAFYFLSLVLKS-IPVGVAYAVWSGLGVVIITAIAWLLHGQKLDAWGFVGMGLI
MMR_MYCTU/1-94   (43%) MIYL---YLLCAIFAEVVATSLLKS-------TEGFTRLWPTVGCLV---GYGIAFALLALSISHGMQTDVAYALWSAIGTAAIVLVAVLFLGSPISVMKVVGVGLI
Y4NH_RHISN/1-106 (28%) MNAVPIILVFAAGLNSCIGNILLKWGRASLPPSAGLADTFLTPGFVGGVVFYGINVLLFAKALDS-LEVSVAYPILAGSGFAMLIIASHYFFGEPFHLHKWIGVALV
```

Fig. S7. Sequence alignment of $EmrE$ **homologs.** 15 representative seed sequences for Multi_Drug_Res (PF00893) family are used.(4, 5) Percentages following sequence names indicate the sequence identity to $E.\ coli\ EmrE$. Residues whose conservation is interpreted in Sec. in light of the present structure are highlighted in red.

X-ray structure of *EmrE* with side chains added using Modeller by Eswar et al. (9) because the Thr side chain appeared to have significant exposure to lipid,(5) suggesting that it was oriented away from the protein. However, in the present equilibrated structure,

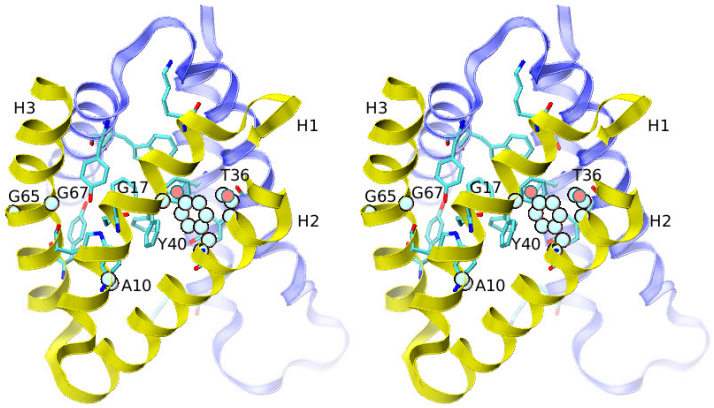

Fig. S8. Stereo view of the *EmrE* **dimer.** The positions of conserved residues discussed in the text are highlighted. Sidechain atoms of these residues are drawn as spheres. Active site residues and TPP are drawn as sticks, and are not labeled. Helices H4 are omitted for clarity.

the T36 side chain is directly between H1 and H2, so that a mutation to the much bulkier residue Trp could destabilize the helix bundle that forms the active site. In the sequence alignment in Fig. S7, the largest sidechain at this position is Phe, with Thr and Val being the most common. Residue mutations in helix H4 will be discussed below, where we describe the role of H4 as the dimerization domain.

The present structure of the H4 dimerization interface is consistent with mutagenesis experiments on *EmrE* and its homolog *Hsmr* (see Fig. 5). Mutations to residues G90, I94 and G97 yield transporters with impaired activity.(10, 11) The two glycines are buried exactly in the interior of the interface so that the addition of a side would prevent the helices from being in close proximity to achieve strong binding. The isoleucine is also buried in the interface, but not directly between the helices. Moreover, it is approximately in the middle of H4, so that the two I94 side chains interact. A mutation that disrupts this interaction would weaken the affinity of H4 for each other. On the other hand, a mutation of C95 does not significantly affect binding or transport.(5) It is evident from Fig. 5 that the C95 side chain points toward the membrane, and therefore has significant exposure to the lipid, especially on monomer 2, so that even substitutions for a bulky W95 would have little impact on activity.

pKa of active site glutamates. pKa values of the active site glutamates have been estimated to be in the range 7.3–8.5;(12, 13) both estimates provide a single effective pKa value. Soskine et al. (12) measured the proton release upon addition of TPP to a single-carboxyl mutant of *EmrE* at different initial pH values, and took the pKa to be the pH at which the proton release was half-maximal. They obtained the value 8.5. Adam et al. (13) used the fact that the addition of TPP to a single Trp63 *EmrE* mutant quenches Trp fluorescence intensity. The authors thus measured rates of TPP binding to the *EmrE* mutant as a function of pH. The data were fit to a model in which TPP binds to fully deprotonated *EmrE*, and the pKa was essentially the pH at which the binding rate is half maximal. The value obtained was 7.3. Because the differences in the environments of E14[1] and E14[2] described above for ligand-free *EmrE* are reflected in the pKa's of their corresponding side chains, masurements of the individual pKa's would be of great interest. In recent solution NMR experiments, Morrison et al. (14) studied the pKa's of the two E14 residues. Because the interpretation was limited by a macroscopic model of deprotonation,(15) it was not possible to determine the pKa values of the individual E14s. Specifically, Morrison et al. (14) measured two different macroscopic pKa values at two temperatures: pKa_I=7.0 *vs.* pKa_{II}=8.2 at 45°C and pKa_I=6.8 *vs.* pKa_I=8.5 at 25°C. The measured values Ka_I and Ka_{II} can be written in terms of microscopic Ka's as

$$\begin{aligned} Ka_I &= Ka^0_{E14[1]} + Ka^0_{E14[2]}, \\ \frac{1}{Ka_{II}} &= \frac{1}{Ka^{-1}_{E14[1]}} + \frac{1}{Ka^{-1}_{E14[2]}}, \end{aligned} \qquad [1]$$

where the subscripts indicate the residue being deprotonated, and the superscripts 0 and −1 indicate whether the E14 on the *other* monomer is protonated or deprotonated, respectively. Equations (1) are constrained by the equilibrium relation $Ka^0_{E14[1]}Ka^{-1}_{E14[2]}$=$Ka^0_{E14[2]}Ka^{-1}_{E14[1]}$, which leaves a system of two equations in three unknowns. In particular, the cases (i) $Ka^0_{E14[1]} \simeq Ka^0_{E14[2]}$, (ii) $Ka^0_{E14[1]} \simeq Ka^{-1}_{E14[1]}$, or (iii) $Ka^0_{E14[1]} \gg Ka^{-1}_{E14[2]}$, which correspond, respectively, to the E14s being identical and protonating cooperatively, the E14 being non-identical but protonating independently, or to the E14s having very different microscopic pKa's, are mathematically compatible with Eq. (1). While Morrison et al. (14) did not assign specific pKa values to the monomers, they hypothesized on the basis of the asymmetry in the NMR spectra and the low-resolution X-ray structure(16) that the E14 occupy different environments, but also protonate anticooperatively ; *i.e.*, they favored the second alternative.

Simulation structures of stapled peptides. Two of the staples that had the highest affinity are shown in Fig. S9a,b, corresponding to N-terminal staple locations A87 and I88. Staples A87 and I89 corresponds to high-affinity peptides with contacts between the staple and the *EmrE* monomer. Staples I88 and M92 preserve the interactions between hydrophobic residues of the stapled peptide and H4 of the *EmrE* monomer, with the staples pointing almost directly away from the H4 binding interface. The peptides with

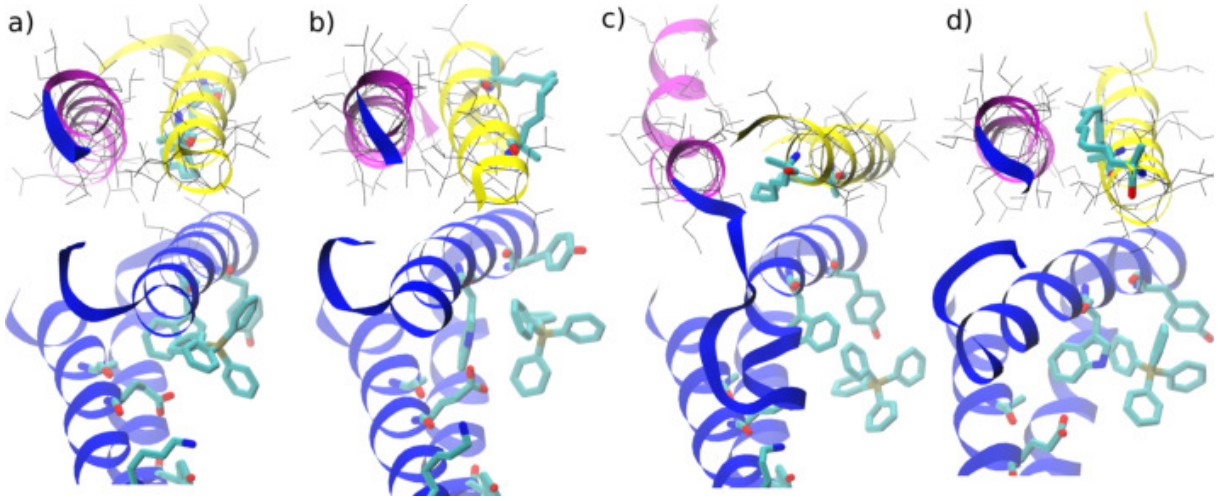

Fig. S9. Binding interface between *EmrE* **monomer and four representative stapled peptides.** Each peptide is identified below by the N-terminal location of stapling a) staple A87 (high-affinity); b) staple I88 (high-affinity); c) staple I94 (low-affinity); d) staple G97 (low-affinity). The stapled peptide is in yellow and the *EmrE* monomer is in blue, except for helix H4, which is in purple; staples are drawn in thick lines and residue side-chains of H4 and the stapled helices are drawn in thin lines.

the lowest affinity correspond to staple locations G90, I94 and G97 (Fig. S4c,d) . The binding free energy was not computed for staple G90 because it spontaneously dissociated from the monomer. The low-affinity staples I94 and G97 disrupt the binding interface (Fig. S4c,d); staple I94 exhibits partial dissociation. Stapling at positions A96 and G97 entail mutations to C-terminal residues L103 and L104, whose side chains are involved in nonpolar interactions with H4 of the monomer.

SI Methods

Computer side-chain modeling and refinement. Two low-resolution ∼4Å structures of dimeric *EmrE* with bound Tetraphenylphosphonium (TPP) were obtained from the Protein Data Bank (codes 3B5D and 3B62).(16) Only C_α carbon atoms were provided at the low resolution. The two structures are very similar (populating different crystal forms), and structure 3B5D was chosen because it is at a slightly higher resolution (3.8Å vs 4.5Å). Starting from the C_α coordinates, the complete protein backbone was generated using CHARMM(3, 17) Experimentally unresolved C-terminal residues 106–110 were not included in the modeling, but the shorter N-terminal missing backbone comprised of res. 1–3 was modeled in CHARMM using standard internal coordinate values for an extended chain. Because side chain coordinates were not available at this step, the backbone was optimized by treating the protein as a poly-glycine chain. Starting from the backbone scaffold, different algorithms were used to construct side-chain conformations for subsequent refinements. These were SCWRL,(18) OPUS-Rota,(19) PDBHydro,(20) and Modeller.(9) The complete models were energy-minimized using the IMM1 implicit membrane model,(21) and used to start Molecular Dynamics (MD) simulations described below. The ligand TPP from the crystal structures was added at this stage. Because TPP is not a widely encountered molecule, this required the development of CHARMM-compatible force field parameters. Initial parameters were obtained from the CGENFF(22) server www.paramchem.org, and were refined using quantum mechanical simulations according to published protocols.(22, 23) The FF-Toolkit(24) was used to facilitate parametrization. The parameters and topology for TPP are provided in an online dataset.(25) **Because TPP was bound to the dimer, and that fact that biochemical studies indicate that the addition of substrate to detergent-solubilized *EmrE* releases about one proton per monomer, the active site glutamates were modeled in the deprotonated state.**

Molecular dynamics simulations for refinement of structures. To obtain realistic *EmrE* structures from the models prepared in 1a, MD simulations were employed in implicit and in explicit solvation. For explicit solvent MD, patches of DMPC lipid bilayers were obtained from CHARMM-GUI,(26) and the protein structures were inserted into the membrane by deleting the lipids that overlapped with the protein. Structures were solvated using the TIP3P water model and equilibrated for 100ns at standard pressure and temperature with weak harmonic restraints applied to the C_α carbons of *EmrE*. During this step, restraints were also applied to the water molecules to keep them away from the membrane interior while the lipid packed around the protein (this functionality was implemented as a Tcl script for the ACEMD(27) GPU-accelerated MD program).

In all of the initial explicit solvent simulations started directly after side-chain modeling and energy minimization, we observed evidence of poor starting simulation structures, *e.g.* a slow separation of *EmrE* helices or monomers, water entry into the binding site, or local unfolding or distortions of helices. The experimentally-measured binding of TPP at pH 7 is strong ($K_D \sim$ 50nM(28)), and is believed to involve both monomers, which would make them unlikely to separate. Also, excessive hydration of the binding pocket could compromise the proton-powered efflux of TPP by compromising the proton gradient. In addition to the qualitative observations, we compared the root-mean-square (RMS) fluctuations computed from the MD simulations with those obtained from the PDB B-factors. The experimental and simulation data correlated with the Pearson coefficients of 0.4 – 0.65 (averaged over the two monomers), which can be compared with the corresponding value of 0.76 from the final refined structure (see Fig. 1f). The simulation structure built

using PDBHydro was excluded from further consideration because of poor inter-helix side chain packing within *EmrE* monomer 2, which caused the corresponding helices to separate by ∼4Å during MD.

To improve the starting structures for the explicit-solvent simulations, an intermediate refinement step was added. The electron density (ED) map corresponding to the 3B5D Xray crystal structure was obtained from Prof. Geoffrey Chang. Restraints to a smoothed ED were incorporated into MD simulations with the enhanced sampling method Self-guided Langevin Dynamics (SGLD).(29) These calculations were performed in IMM1 implicit solvent(21) with CHARMM. Furthermore, under the influence of the ED restraints, the structures were alternately heated to 600K and quenched to 300K five times for 1ns per simulation (with 10ns of total time) to help the side chains adopt conformations that are most compatible with the ED.

During the simulations, both, the quality of the fit to the map improved, and average energy of the structures decreased, suggesting that the equilibrated structures are more consistent with the ED. The most energetically stable structure corresponds to the one initially generated using Modeller(9) using the C_α PDB structure as the template.

Evaluation of refined and equilibrated structures. The lowest-free energy structure from step 1b was immersed in a solvated DMPC bilayer, and equilibrated for 100ns in the NPT ensemble with harmonic restraints to the starting structure (as above). Because ED restraints were already incorporated into the equilibration simulations in 1b, they were not used in this step. Restraints to prevent water from entering the membrane were turned off after 50ns, harmonic restraints on the protein were turned off at 75ns, and the barostat was turned off at 100ns to speed-up subsequent production simulations. 12Å cutoffs were used in all simulations, in accordance with the lipid force-field.(30) A 1μs MD simulation was performed using GPU hardware.(27) The protein remained stable during the simulation, but the RMSD from the initial C_α structure exhibited a slow increase from ∼2.4Å to ∼3Å. Inspection of the MD trajectory revealed a lipid tail intercalated between helices 2 and 3 of monomer 1, which was causing separation between the helices. RMSD recomputed using only the coordinates of monomer 1 showed a gradual increase, but that recomputed using only the coordinates of monomer 2 showed a plateau after ∼500ns.

Because monomer 2 was stable in the simulation, we replaced the coordinates of the first three helices of monomer 1 with those of monomer 2 (after a best-fit superposition of the latter onto the former). The fourth helix was left in place because it appeared stably packed to that from monomer 2 (see *e.g.* Fig. 5), and functions as a dimerization motif.(16, 31) The RMSD of the superposed monomers was 1.8Å, and the fit was of sufficient quality that the positions of any other atoms including lipids, residue side chains, or waters, did not need to be altered manually. The resulting structure (including the lipids, waters, and a neutralizing Cl^-) was minimized for 4500 minimization iterations in CHARMM, with restraints on the protein atoms gradually switched off, and the MD simulation was continued for 1μs.

The results showed that the protein remained stable with an RMSD plateau of ∼2.75Å from the initial structure (see Fig. 1e). Monomer 1 undergoes minor rearrangements in the first 250ns of the simulation, with its RMSD from the starting structure initially increasing to ∼3Å, and subsequently falling to ∼2.5Å. Examination of the MD trajectory showed that the rearrangements correspond to monomer 1 approaching more closely to monomer 2, and forming a tighter binding pocket for the TPP ligand.

MD simulations of apo-*EmrE* in different protonation states. Starting from the refined structure produced with the methods described above, TPP was deleted to produce the ligand-free apo state, fully deprotonated on both E14. This state was simulated by MD for 900ns in the NVT ensemble, using the MD simulation parameters described above. In three parallel studies, the E14 residues were protonated only on monomer 1, only on monomer 2, or on both monomers, and MD simulations were performed for 350ns in each case. The reason for the longer MD simulation length in the case of *EmrE* fully deprotonated at E14, is that significant structural changes were observed in the simulation, which required a longer equilibration transient to reach steady-state behavior in the RMSD evolution.

MD simulation of *EmrE* bound to ethidium cation. Starting from the refined structure of *EmrE* with bound TPP, we removed TPP and inserted ethidium in its place in a random orientation, with the position of the COMs of ethidium set to that of TPP. To optimize the orientation of ethidium, atoms that were a distance of 18Å or greater from ethidium were fixed, and the remaining atoms excepting hydrogens, ethidium atoms, and side chain atom pairs with planar symmetry, were harmonically restrained to their initial positions with force constant 0.5 kcal/mol/Å^2. The reason for using weak force constants was to allow flexibility in the active site residues, while biasing the residues to their equilibrium positions in the presence of TPP. The reason for excepting side chain atoms related by symmetry was to allow greater conformational flexibility. While we did not observe ring flips during high-temperature equilibration, we did observe flips of carboxylic oxygens O_ϵ of E14.

The structure was minimized in the presence of the above restraints and constraints using 100 iterations of the ABNR minimizer in CHARMM(17), and the structure was simulated at 900K and then at 300K, for 100ps each, using the Langevin thermostat coupled to ethidium with the friction of 1/ps. The high temperature MD allowed the ethidium molecule to sample a broad range of orientations; the final orientation of ethidium at the end of the 300K simulation differed from the initial placement by 2.75Å. The final structure was simulated by MD in the NVT ensemble for 1μs, using simulation parameters described previously. CHARMM-compatible force field parameters for ethidium were obtained from CGENFF(22) *via* www.paramchem.org. Charges were optimized using FF-Toolkit(24); bond, angle and dihedral parameters were not optimized because ethidium is a relatively rigid molecule, (*e.g.* RMSD conformational fluctuations at 300K were ∼0.5Å) and because the majority of the initial parameters had low penalty scores (less than 5). The parameters are provided in an online dataset.(25) Shorter simulations were performed with ethidium inserted in different orientations, all of which resulted in essentially the same binding pose within several nanoseconds.

Design of stapled peptides. Starting from the refined structure of *EmrE*, monomer 1 was deleted, except for helix H4, which provided the template for the stapled helices. The resulting system was equilibrated to close the space vacated by the deleted helices. The

protein C_α atoms were restrained to their positions, with harmonic restraints using a force constant of 0.5 kcal/mol/Å^2. Water molecules were prevented from penetrating the membrane using one-sided potentials implemented as a Tcl script, as done before. A Berendsen barostat was used with a relaxation time of 10,000 steps to allow the simulation box to reshape according to the new composition. A Langevin thermostat was used to maintain temperature at 298K with the friction of 0.1/ps. Restraining potentials acting on water molecules were turned off after 15ns, those acting on protein atoms were turned off after an additional 20ns, and the barostat was turned off after an additional 20ns. The simulation was continued in the restraint-free NVT ensemble for 1μs. During the equilibration the remaining *EmrE* monomer underwent significant structural changes (see *Results*) with the backbone RMSD from the starting conformation of ∼3Å. However,the RMSD computed on the basis of H4 backbone atoms only was ∼0.9Å, further underscoring the stability of the dimerization motif (see *Results*). The equilibrated structure was the starting point for stapled peptide structures. Hydrocarbon staple spanning two turns of H4, corresponding to residue pairs (i,$i+1$) were generated at positions corresponding to i=86, . . . , 97.(32) Initial staple coordinates were taken from the stapled p53 peptide bound to MDM2.(33) Essentially, the staple is a hydrocarbon chain linking the C_α carbons of two residues (see Fig. 6a and Table 4 in *Results*). CHARMM-compatible parameters for the staples were generated by combining the amino acid parameters with hydrocarbon parameters (butene or propene) from the corresponding CHARMM36 force fields.(34, 35) The stapling was implemented by first defining new protein residues for the N-terminal and C-terminal ends of the staple, followed by application of a linker (CHARMM *patch*) to the two residues. The staple parameters are provided in an online dataset.(25)

The staple atoms did not show significant steric clashes with lipid atoms, and therefore no lipid molecules were deleted. Each *EmrE*-peptide structure was minimized extensively using CHARMM prior to MD simulation. All protein coordinates except for those of the stapled residues were fixed, and harmonic restraints were applied on the remaining atoms. The harmonic force constant k was set to 10^i kcal/mol/Å^2 with i decreasing from 6 to 0 in steps of −1. At each value of k, three minimizations were performed using Steepest Descent, Conjugate Gradient, and Adaptive-Basis Newton-Raphson minimizers, for 10 steps each. The resulting structures were equilibrated for 20ns in the NPT ensemble (using the barostat and thermostat parameters described above) in the presence of harmonic restraints on the C_α protein atoms with the force constant of 0.5 kcal/mol/Å^2. The restraints and the barostat were switched off, and the staples were simulated for 100ns. The structure corresponding to staple position i=90 was not retained for further consideration because the stapled peptide separated from H4 of the *EmrE* monomer due to steric clashes. The eleven remaining structures, along with the structure with the unstapled helix for use as a reference model, were retained for free energy analysis.

Free energy simulations of TPP binding to *EmrE*. Using the refined structure, alchemical free energy (FE) simulations were performed to evaluate the binding of the ligand TPP to *EmrE* using reversible annihilation of TPP in the *EmrE* binding pocket, and in a water box of the same dimension as that used for the *EmrE*/TPP complex. FE perturbation (FEP) simulations were carried out using the program NAMD(36) and analyzed using the ParseFEP Toolkit.(37) Forward and backward FE simulations were performed, and the FE difference computed using Bennett acceptance criterion.(38) Each simulation was split into 40 equispaced windows. Clustering of windows near the annihilation point of TPP was not necessary because we used a 'soft core' potential, which avoids end-point singularities in the standard nonbonded potential that occur when an annihilated molecule appears in a region of space partly occupied by other atoms. For TPP in the protein, 3ns of MD simulation were performed for each window in each direction (annihilation and creation), and for TPP in water, 600ps of MD were performed for each window. In each window of the simulation in water, the first 100ps of data were discarded as part of equilibration. In each window of the simulation in *EmrE*, 1.5ns were discarded. The simulation time in water was less than that in *EmrE*, but the statistical errors were similar for the two simulations (∼0.14 kcal/mol).

To improve convergence, orientational and conformational restraints were applied to TPP, which were similar in spirit to those described by Boresch et al. (39) and Gumbart et al. (40) Specifically, a mass-weighted RMSD restraint was imposed in each simulation to limit motions of TPP. For TPP in water, restraint forces were applied to all TPP atoms after the COM of the reference TPP coordinates was superposed onto that of the TPP simulation coordinates. Because this RMSD restraint does not include rotational alignment, the FE change of imposing the restraint explicitly includes the contribution from rotational entropy of TPP.

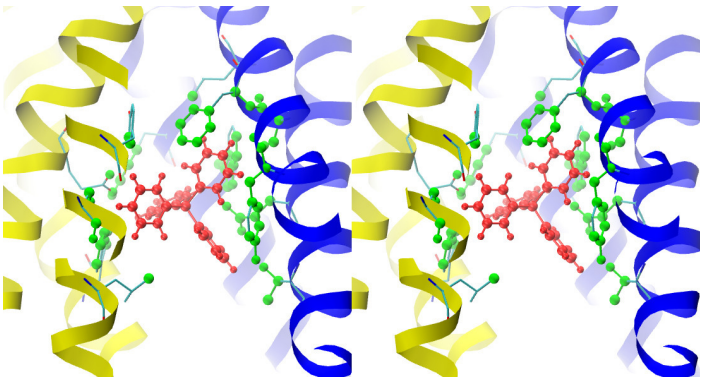

Fig. S10. Atoms used to define the RMSD restraint to confine TPP to the active site of *EmrE*. The orientation (active site) atoms are in green, and atoms based on which the RMSD was computed (*i.e.* TPP) are in red. Residues that contain at least one orientation atom are drawn as lines.

For TPP in *EmrE*, restraint forces were applied to all TPP atoms after a rotation that superposed the reference coordinates of the *EmrE* active site onto those of the simulation structure; The active site was defined as all heavy atoms that were within 4Å of TPP,

not including TPP, which results in the set of 60 atoms shown in Fig. S10 and listed in Tab. S3. This RMSD potential restrains the position and the orientation of TPP relative to the active site in the reference structure, as well as the internal configuration of TPP. The FE change of imposing this restraint therefore includes contributions from the translational and rotational entropy loss associated with confining TPP to a single conformation within the active site of *EmrE*. Because the translational entropy contribution is missing from the RMSD restraint imposed in the solvent (see above), the well-known analytical correction is included in the expression for the standard binding FE,(41) which is

$$\Delta G_{\mathrm{Tr}} = -k_B T \log V_0 \left(\frac{k_{RMSD}}{2\pi k_B T}\right)^{3/2}, \quad [2]$$

where the volume V_0=1661Å^3 corresponds to the standard concentration of 1M, and the positional force constant equals k_{RMSD} (2.275474 kcal/mol/Å^2 from Tab. S1) because of the separability of translational degrees of freedom from the remaining (rotational and configurational) ones.

The RMSD restraints were applied in NAMD using a modified version of the Free Energy Restraints (FER) module. The implementation of the RMSD restraint was described previously by Ovchinnikov and Karplus (43). The FE contribution of imposing the restraints was computed using free energy perturbation. Ten simulation windows were defined, in which the force constant k_{RMSD} in the RMSD restraint potential

$$U_{RMSD} = \frac{k_{RMSD}}{2} \times \rho_m^2(\boldsymbol{X}, A(\boldsymbol{X}, \boldsymbol{X}_0)\boldsymbol{X}_0), \quad [3]$$

varied exponentially, as listed in Tab. S1. In Eq. (3), ρ_m^2 is the mass weighted mean-squared-distance (MSD) between an instantaneous configuration $\boldsymbol{X}$ and the reference (starting) configuration $\boldsymbol{X}_0$ to which a rotation A is applied, *i.e.*,

$$\rho_m^2 = \frac{1}{M}\sum_{j=1}^{N} m_j \|X_j - AX_{0j}\|^2. \quad [4]$$

Masses of the N=45 restrained TPP atoms are denoted by m_j, atomic coordinate triplets, by X_j, $M = \sum_{i=1}^{N} m_j$, and the possible dependence of the rotation A on $\boldsymbol{X}$ and $\boldsymbol{X}_0$ is omitted for brevity. The rotation A is typically taken to be the rotation that minimizes the MSD between the coordinates $\boldsymbol{X}$ and $\boldsymbol{X}_0$, in which case it corresponds to best-fit rotational alignment.(44) If rotational best-fitting is not desired, as in the simulation of TPP in water, in which the rotational entropy contribution was included in the reversible work of imposing the restraint, A is set to the identity matrix. Generally, A can be defined to perform an alignment of atoms different from those based on which the RMSD is computed (as in the simulation of TPP in *EmrE*, where the protein atoms in the *EmrE* active sites were taken as the basis for alignment, while the RMSD was measured using TPP atoms). The coordinates are implicitly shifted to the COMs of the appropriate group prior to the computation of the RMSD. This group was TPP for TPP in water, and the active site protein atoms for TPP in *EmrE*. Further discussion of the rotation A can be found in Ref. 43.

For each restraint window, the system was simulated for 1ns. Restraint energy U_{RMSD} was output from the simulation every 0.1ps, and the restraint free energy was computed using the ParseFEP Toolkit.(37) All NAMD simulations were performed in the NPT ensemble, with the nonbonded cutoff of 12Å, using CHARMM-style van der Waals switching function for interatomic distances above 10Å. The Langevin thermostat was used to maintain simulation temperature at 300K, with the friction of 1/ps on all atoms, and the Berendsen barostat was used to maintain simulation pressure at 1atm, with the relaxation time of 500ps. Long-range electrostatic forces and barostat forces were updated every other simulation step using multiple time stepping, and the simulation time step was 1fs.

An additional potential contribution to the standard binding FEs arises from the symmetry of TPP.(39) For TPP in the protein, the required correction might appear to be $\Delta G_{\mathrm{Symm}} = -k_B T \log \sigma_{TPP+}$, where σ_{TPP+} is the symmetry factor of TPP, equal to $4! \times 2^4$. The factorial arises from the number of ways to arrange four identical groups (in this case, phenyl rings) around the central phosphorous atom for a tetrahedral geometry, and 2^4 arises from the fact that each of the four phenyl rings can be rotated by 180 degrees along a line through the phosphorous to generate a physically identical TPP conformation. However, the factor 4! includes configurations that are related by reflections, which would correspond to a chirality change if the phenyl rings were distinguishable. Barriers corresponding to chiral flips are very large in classical force fields because they proceed through high-energy planar intermediates; we observed them neither with TPP in water, nor bound to *EmrE*. Therefore, the relevant part of the symmetry factor is $4 \times 3 \times 2^4$, which corresponds to the FE correction

$$\Delta G_{\mathrm{Symm}} = k_B T \log 192 = 3.11 \text{ kcal/mol}. \quad [5]$$

The individual contributions of free energy components to the standard binding free energy are listed in Tab. S2.

Free energy of association between *EmrE* and stapled peptides. Free energies of association between the *EmrE* monomer and the stapled peptides were computed using flat-bottom restraints,(45) supplemented with orientational and translation restraints implemented as part of the string method code.(46) The procedure is illustrated qualitatively in Fig. S12.

First, for each *EmrE*-peptide complex, a reaction coordinate (RC) was chosen as the displacement along the vector pointing from the center-of-mass (COM) of helices 3 and 4 of the *EmrE* monomer to the COM of the stapled peptide, with the transmembrane component of the vector set to zero. The stapled helix was reversibly separated from *EmrE* along the RC, with the final displacement of 12Å. The inclusion of helix 3 of *EmrE* was to ensure that the stapled helix would not be able to remain close enough to interact with any part of *EmrE* after the separation. The RC was discretized into 15 windows with displacements given by the stretched grid $(i/15)^{1.2} \times 12$Å, where i is the window index $i \in \{1, \ldots, 15\}$. The stretched grid provides higher resolution in the region where the potential of mean force (PMF) along the RC is increasing rapidly, and the lowest resolution in the region where the stapled peptide is

i	k_{RMSD}	i	k_{RMSD}
1	0	6	0.174605
2	0.013398	7	0.331750
3	0.025456	8	0.630325
4	0.048367	9	1.197618
5	0.091898	10	2.275474

Table S1. Restraint force constants used in FEP simulations. The force constants are exponentially distributed.(42) Units are kcal/mol/Å^2.

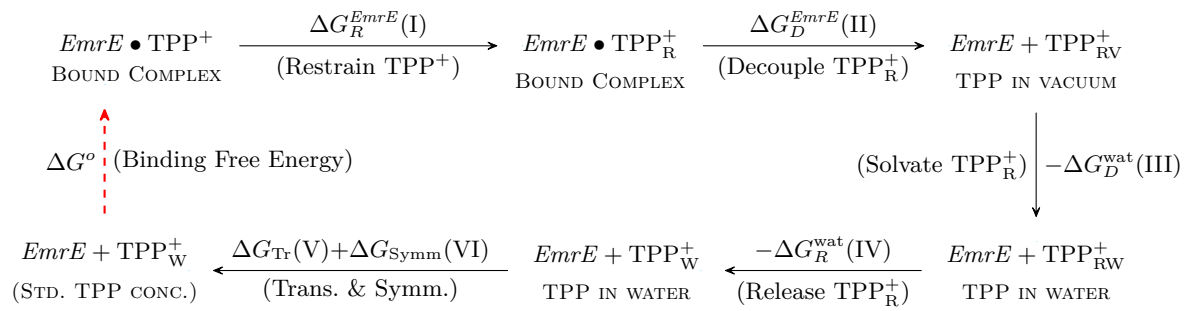

Fig. S11. Alchemical free energy cycle for computing the standard free energy of TPP binding to $EmrE$**.** The desired binding process is indicated by the dashed red arrow. Because the free energy is a function of state, the quantity ΔG^o can also be computed *via* the successive transformations indicated by the black arrows. A negative sign preceding a free energy difference indicates that the value was computed for the reverse process for the sake of convenience (e.g. annihilation *vs.* exnihilation). $\Delta G_{\rm Tr}$ and $\Delta G_{\rm Symm}$ refer to the translational and symmetry contributions, which are given analytically (see text). The values for the free energy changes ΔG(I–VI) are listed in Tab. S2.

ΔG_R^{EmrE}(I)	ΔG_D^{EmrE}(II)	$\Delta G_D^{\rm wat}$(III)	$\Delta G_R^{\rm wat}$(IV)	$\Delta G_{\rm Tr}$(V)	$\Delta G_{\rm Symm}$(VI)	ΔG^o
1.33±0.01	33.5±0.6	18.3±0.3	5.47±0.06	-3.97	3.11	-10.3±0.7

Table S2. Contributions to the standard free energy of TPP binding to $EmrE$**. The corresponding thermodynamic cycle is shown in Fig. S11.**

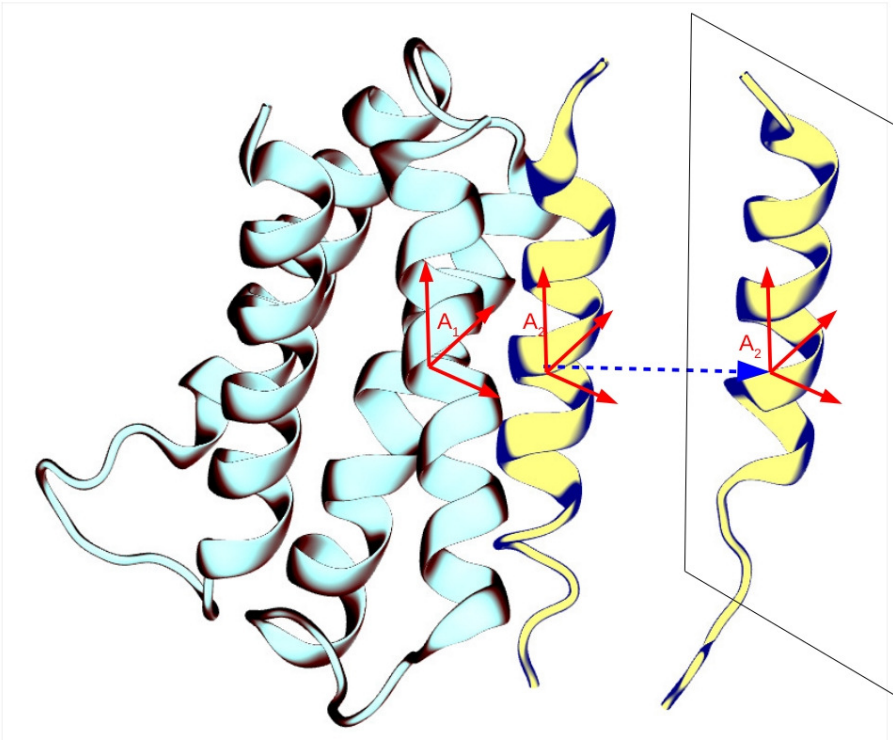

Fig. S12. Schematic of the procedure used to compute FEs of association between $EmrE$ **and peptides.** Starting from an $EmrE$ monomer/peptide complex, the peptide is displaced away from the monomer (cyan) along the vector that points from the COM of helices 3 and 4 of the monomer to the COM of the peptide (yellow). The initial and final positions of the peptide are shown. To preserve the relative orientation of $EmrE$ and the peptide, a restraint on an orientation quaternion is used. Specifically, the quaternion corresponding to the rotation $A_1 A_2^T$ is harmonically restrained, where A_1 and A_2 are the coordinate vectors formed by the principal components of the monomer and the peptide, respectively. The rectangle around the displaced peptide qualitatively indicates the region perpendicular to the displacement coordinate within which the peptide is allowed to move freely, using flat-bottom harmonic potentials.

well-separated from *EmrE*. The width of the flat-bottom region of the restraint potentials was 0.5Å, and the restraint force constant was 20 kcal/mol/Å^2.

To accelerate convergence of the mean force, conformational sampling was limited by use of restraints, as follows. To limit conformational fluctuations of *EmrE*, the C_α atoms in the monomer were restrained to their positions with harmonic restraints with force constant k=1 kcal/mol/Å^2. To limit the orientational and rotational freedom of the stapled peptide relative to the *EmrE* monomer, two local coordinate systems were defined (A_1, $A_2 \in M_{3\times3}$), as described before(46, 47), one using all carbon atoms of helices 3 and 4 of *EmrE*,

and another, using all carbon atoms of the stapled helix. (Using only the C_α or backbone atoms of a helix or a helical bundle is not sufficient to define a local coordinate system because of the approximate radial symmetry of the helical backbone.) The orientational motion of the stapled helix was limited by applying harmonic restraints to the quaternion associated with the superposition of the two coordinate systems, which corresponds to the matrix product $A_1 A_2^T$. The quaternion restraint force constant was 1000 kcal/mol, applied to each quaternion component. The motion of the stapled helix was restrained by restraining the coordinates of the COM of the stapled helix in the plane perpendicular to the RC, using flat-bottom potentials with width 5Å in each of the two perpendicular directions. The restraints were implemented in C and FORTRAN using the plugin interface to ACEMD.(27)

The simulations corresponding to the 15 windows were performed sequentially, starting in window 1, using the coordinates of the previous window (or the initial model coordinates for the first window) to initialize the simulations. The simulations were run until the potential of mean force computed using the third and fourth quarter of the entire simulation data differed by less than 1 kcal/mol. On the average, this required about 40ns per window, corresponding to 600ns of MD simulation per staple. To accelerate the FE simulations, the nonbonded cutoff was set to 9Å, the switching function was nonzero above 7.25Å, long-range electrostatics were evaluated at every other simulation step, and, hydrogen masses were set to 4 a.m.u., which allowed the use of a 4 fs time step. The aggressive simulation parameters are justified in this case because the purpose of the FE simulations was to rank the stapled peptides *relative to each other* according affinity for *EmrE*. Since all of the peptides were simulated using identical parameters, we expect any significant errors to cancel when affinity differences are considered.

To compute an approximate standard binding free energy, we need to account for (i) the orientational freedom of the peptides lost due to the use of the orientational restraints, and (ii) the concentration of the unbound peptides. The rotational contribution to the free energy is approximated using the rigid rotor formula(48)

$$\Delta G_{\rm rot} = -k_B T \log\left[\frac{1}{h^3}\sqrt{\pi}\,(8\pi k_B T)^{3/2}\,|I|^{1/2}\right], \qquad [6]$$

where $|I|$ denotes the determinant of the moment of inertia tensor of the molecule and h is Planck's constant. Strictly speaking, $\Delta G_{\rm rot}$ consists of three contributions, *i.e.*,

$$\Delta G_{\rm rot} = \Delta G_{\rm rot}^{EmrE} + \Delta G_{\rm rot}^{peptide} - \Delta G_{\rm rot}^{EmrE+peptide}, \qquad [7]$$

where *EmrE* is the monomer bound to the peptide. However, because the monomer is much larger than the peptides, $|\Delta G_{\rm rot}^{EmrE+peptide} - \Delta G_{\rm rot}^{EmrE}| \simeq 0.015$ kcal/mol, which is much smaller than the accuracy of the FE calculations. Therefore one can consider the *EmrE* as being fixed, and simply use

$$\Delta G_{\rm rot} \simeq \Delta G_{\rm rot}^{peptide}. \qquad [8]$$

The average value of $\Delta G_{\rm rot}$ was -13.1±0.01 kcal/mol computed from the initial peptide structures.

The concentration correction is given by the logarithm of the accessible volume ratio

$$\begin{aligned}\Delta G_{\rm conc} = &-k_B T\,(\log 1661 \\ &- \log[5 + (2\pi k_B T k_{\rm res}^{-1})^{1/2}]^2 \\ &- \log[0.5 + (2\pi k_B T k_{\rm res}^{-1})^{1/2}]\big) \\ \simeq &-2.5 \text{ kcal/mol},\end{aligned} \qquad [9]$$

where the first logarithm is the standard volume per molecule, and the remaining logarithms are composed of the volume contributions form the flat bottom region of the restraint potential (5×5×0.5Å^3), and from the Gaussian integrals associated with the harmonic potentials. The the restraint force constant is $k_{\rm res}$=20 kcal/mol/Å^2.

pKa shift calculations. To compute the pKa of active site residues E14 in ligand-free *EmrE*, we used Poisson-Boltzmann (PB) solvation theory, as implemented in the program APBS.(49) The FE difference was used to calculate the pKa shift in *EmrE* relative to the pKa value of E14 side chain in bulk water, taken to be 4.3.(50) To take into account conformation flexibility of *EmrE*, structures were taken from the equilibrium MD trajectories of *EmrE* without ligand, in 20ns increments. Three trajectories were considered; two with *EmrE* singly protonated on E14[1] and E14[2], and one with *EmrE* doubly protonated on both glutamates.

For each protonated glutamate, additional structures can be generated by rotating the carboxyl group by 180° around the bond formed by the carboxyl carbon and its antecedent carbon (C_γ–C_δ bond). This operation reflects the fact that glutamates can be protonated on either carboxyl oxygen. Although this operation could be used to obtain better statistics, we did not pursue this approach because spontaneous rotations of the E14 side chains were observed in the simulation trajectories, indicating that the statistics include contributions from both rotamers. For the computed pKa's we report the value computed from the Boltzmann average of the free energy change associated with the deprotonation.

The dielectric constants of the protein, lipid and water were set to 2, 1, and 78.5, respectively, and grid resolution was 0.625, which typically corresponds to maximum errors of 2–3%, compared to solutions on a much finer solution grid.(51) The protein and lipid dielectric constants are lower than typical values (2–20),(52) with most common values near 4,(53) because larger values are typically chosen to account for conformational flexibility around a single structure, in addition to electronic polarization. Since an ensemble of instantaneous structures generated by MD was used here, conformational flexibility is explicitly taken into account.

Peptide synthesis, purification and quantification. Peptides were synthesized on an automated PS3 peptide synthesizer (Protein Technologies Inc., AZ, USA) using standard solid state Fmoc (N-(9-fluorenyl)methoxycarbonyl) and HATU (1-[Bis(dimethylamino)methylene]-1H-1,2,3-triazolo[4,5-b]pyridinium 3-oxid hexafluorophosphate) (Novabiochem, ON, Canada) chemistry on a low-load PAL-PEG resin (Applied Biosystems, CA, USA) that produced an amidated C-terminus after cleavage. Coupling times were 30 minutes X 2. The initial lysine residue, all beta-branched amino acids (Val, Ile), and those that followed in the sequence were double coupled. The incorporation of staple precursor amino acids, (S)- N-Fmoc-2-(4'-pentenyl)alanine (Fmoc-S5Ala-OH) and (R)- N-Fmoc-2-(7'-octenyl) alanine (Okeanos Technology Co., Beijing, China), was performed as previously described.(54) Briefly, Fmoc-R8Ala-OH and Fmoc-S5Ala-OH amino acids were coupled manually for 2 hours in a 7:3 (v/v) mixture of DMF:DCM (dimethylformamide: dichloromethane) supplemented with Pyclock (6-Chloro-benzotriazole-1-yloxy-tris-pyrrolidinophosphonium hexafluorophosphate) (Novabiochem, ON, Canada) and DIEA (*N,N*-Diisopropylethylamine). Amino acids following Fmoc-R8Ala-OH and Fmoc-S5Ala-OH were double-coupled on the machine with a 30 minute X 2 coupling time with Pyclock (222 mg) substituted for HATU. Olefin ring closing metathesis was performed on resin using 8 mg Grubbs 1st generation catalyst (Sigma-Aldrich, ON, Canada) dissolved in 2 mL DCE (dichloroethane) and reacted for 2 hours with mixing under a N_2 stream. The reaction was repeated twice to ensure full stapling. The final N-terminal Fmoc protecting group was then removed and peptides were reacted with acetic anhydride and DIEA in DMF for 1 hour producing an acetylated N-terminus. All peptides were cleaved using a standard TFA (trifluoroacetic acid) cleavage mix (88% TFA, 5 % water, 5% phenol, 2% TIPS (triisopropylsilane) and reacting for 2 hours. Cleaved peptide was precipitated using ether, washed, and lyophilized prior to purification. All peptides were purified using reverse-phase high-performance liquid chromatography (RP-HPLC) with a C4 semipreparative column (250 x 21.20 mm, 300Å pore size, Phenomenex, CA, USA). Lyophilized peptide was dissolved initially in 100% acetonitrile and then diluted to 30% acetonitrile, 70% water prior to injection on the column. The initial mobile phase composition was 60% solvent A (95% water, 5% acetonitrile, and 0.1% TFA) and 40% solvent B (95% acetonitrile, 5% water, and 0.1% TFA) with a flow rate of 4 mL/min. Solvent B was increased to 60% over 10 minutes, followed by introduction of solvent C (95% isopropanol, 5% water, and 0.1% TFA, 1.6 %/min) to a total of 70% with a decrease in solvent A to 0% (0.9 %/min) and solvent B to 30% (0.7%/min). A mobile phase composition of 30% solvent B/ 70% solvent C was held for an additional 10 minutes during which time the peptides eluted. All peptides were purified to a single peak by RP-HPLC, masses confirmed using mass spectrometry. Lyophilized peptides were dissolved in TFE (2,2,2-trifluoroethanol) for quantification. Peptides were quantified using the absorbance at 215 nm and the extinction coefficient 64 833 cm^{-1} M^{-1} as determined from plotting the Abs_{215} of a TM peptide standard in TFE of similar length to the stapled EmrE peptides.

Liposome preparation. 1-palmitoyl-2-oleoyl-*sn*-glycero-3-phosphocholine (POPC) and 1-palmitoyl-2-oleoyl-*sn*-glycero-3-phospho-(1'-rac-glycerol) (POPG) in chloroform (Avanti Polar Lipids Inc., AL, USA) were mixed in a 3:1 mol ratio (POPC:POPG) and dried into thin films. Lipid films were lyophilized overnight and brought up in 1 mL water, vortexed, frozen and lyophilized again. Lipids were then resuspended in 10 mM Tris buffer 10 mM NaCl pH 7.4 (5 mM) and freeze thawed 5X over dry ice and a water bath (50°C). Lipids were then extruded using a 0.2 micron sized filter and left to equilibrate overnight. Samples were diluted further with buffer (2.5 mM) prior to addition to lyophilized peptide.

Circular dichroism spectroscopy. Secondary structure determination was carried out using a Jasco J-720 spectropolarimeter (Jasco Inc., MD, USA). Detergent samples were prepared by adding SDS (sodium dodecyl sulfate) to quantitated peptide dissolved in TFE. Samples were diluted with water, shaken for 15 minutes, frozen, and lyophilized. Lyophilized peptide/detergent powder was dissolved in the appropriate amount of buffer and allowed to equilibrate for 3 hours at room temperature. Peptide concentration was 20 μM in 10 mM Tris buffer 10 mM NaCl pH 7.4, supplemented with 20 mM SDS. Lipid samples were prepared by adding preformed liposomes (2.5 mM; POPC:POPG molar ratio of 3:1) in buffer directly to lyophilized peptide (20 μM) and allowed to equilibrate for 3 hours at room temperature prior to reading. Samples were read using a 0.1cm cuvette path length with 3 accumulations per run and a 50nm/sec scanning speed. Spectra represent the average of three independent replicates. After subtraction of background noise, each spectrum was converted to mean residue molar ellipticity (MRE) using standard formulas.

Growth inhibition assay. *E. coli* K12 cells were grown overnight to saturation in LB (Luria broth). Cells were harvested and resuspended in fresh media to a final OD_{600} of 0.1. Cells were then grown in the presence of DMSO (dimethyl sulfoxide) alone or in DMSO-solubilized peptide (4 μM) over 1 hour, while OD_{600} was recorded in 15-minute intervals. *E. coli* growth curves were normalized to the starting OD_{600}. Growth in the presence of peptide was normalized to the growth of cells with DMSO alone, using

$$Growth = \frac{OD_{600}^{+peptide}}{OD_{600}^{-peptide}}. \quad [10]$$

Ethidium efflux assay. Ethidium bromide (*EtBr*) efflux assays were performed as described previously with slight modifications.(55, 56) *E. coli* K12 cells were harvested by centrifugation, resuspended and diluted to an $OD_{600} = 0.1$ in Minimal Medium A. Cells were then treated with 80 μM carbonyl cyanide m-chlorophenyl hydrazine (CCCP) for 5 min at room temperature, before adding 1 μg/mL *EtBr* and either DMSO (8 μl) or peptide (4 μM) from a concentrated DMSO stock (1000 μM peptide). Cells were incubated at 37 °C with shaking (250 rpm) for 30 min, centrifuged for 10 min, resuspended in fresh Minimal Medium A supplemented with 1 μg/mL *EtBr* (without CCCP). Fluorescence decay was immediately measured using a spectropolarimeter (Photon Technology International, NJ, USA) over 2200s with stirring (λ_{ex} = 530 nm, slit width 2 nm, λ_{em} = 600nm, slit width 4 nm, 1s intervals). Background fluorescence intensity (ethidium alone) was subtracted from fluorescence values. Efflux experiments were repeated a minimum of three times.

To quantify the degree of *EmrE* inhibition by the peptides, we use a minimal model of ethidium transport, which provides a very good fit to the fluorescence decay data (Fig. 7c). First, since the efflux experiments are performed in a solution of *EtBr*, we note that ethidium can diffuse across the membrane passively, along its electrochemical gradient. The passive diffusion together with the active efflux of ethidium by *EmrE* eventually establish an equilibrium intracellular ethidium concentration, which manifest as a fluorescence plateau at long times (Fig. 7c). Second, at the beginning of the efflux experiment, the proton gradient is impaired by CCCP, and we assume that (1) *EmrE* is inactive (since it is a proton-gradient-driven pump), and (2) ethidium concentration is the same inside and outside the cell. These assumptions are consistent with the initial fluorescence plateau (Fig. 7c). As the CCCP diffuses out of the membrane, the *pH* gradient is gradually restored, and *EmrE* efflux increases to its maximum. For simplicity, we model the gradual activation of *EmrE* with the linear ramp function:

$$r(t) = \begin{cases} 0, & \text{for } t < t_0 \\ \gamma(t - t_0), & \text{for } \gamma^{-1} > t - t_0 > 0 \\ 1, & \text{for } t - t_0 > \gamma^{-1}, \end{cases} \quad [11]$$

where t_0 and γ are the start and the slope of the ramp, respectively, fit from fluorescence data. The decrease in intracellular ethidium is modeled as

$$\frac{d[e_i]}{dt} = k_{diff}([e_0] - [e_i]) - k_{eff}^{max} r(t)[EmrE_2][e_i], \quad [12]$$

where k_{diff} corresponds to passive diffusion, k_{eff}^{max} is the maximum efflux rate by *EmrE* after the *pH* gradient is fully restored, $[EmrE_2]$ is the concentration of functional *EmrE* dimers, which is dependent on the degree of inhibition by the peptides, and $[e_0]$ is the extracellular (as well as initial intracellular) ethidium concentration. We assume $[e_0]$ is constant because the volume of cells is very small compared to the volume of the solution at OD_{600}=0.1 (on the order of 0.01 %).

Our aim is to use the fluorescence decay data to obtain $k_{EmrE} \equiv k_{eff}^{max}[EmrE_2]$ for each peptide. The ratios of these effective first-order constants give the relative concentrations of functional *EmrE* dimers in each case, which are determined by the efficacy of the inhibitor peptides.

The analytical solution to Eq. (12) is

$$[e_i](t) = \begin{cases} 0, & \text{for } t < t_0 \\ [e_0]\left[e^{-\alpha(t-t_0)-\beta(t-t_0)^2}\left\{1 - \frac{\alpha}{\sqrt{\beta}} D\left(\frac{\alpha}{2\sqrt{\beta}}\right)\right\} + \right. \\ \left. \frac{\alpha}{\sqrt{\beta}} D\left(\sqrt{\beta}(t-t_0) + \frac{\alpha}{2\sqrt{\beta}}\right)\right], & \text{for } \gamma^{-1} > t - t_0 > 0 \\ [e_0]\left[\left\{\delta - \frac{k_{diff}}{k_{diff}+k_{EmrE}}\right\} e^{-(k_{EmrE}+k_{diff})(t-t_0-\gamma^{-1})} \right. \\ \left. + \frac{k_{diff}}{k_{diff}+k_{EmrE}}\right], & \text{for } t - t_0 > \gamma^{-1}, \end{cases} \quad [13]$$

where we have defined auxiliary constants α=k_{diff}, β=$\gamma k_{EmrE}/2$, and

$$\begin{aligned} \delta =& e^{-\alpha(t-\gamma^{-1})-\beta(t-\gamma^{-1})^2}\left\{1 - \frac{\alpha}{\sqrt{\beta}} D\left(\frac{\alpha}{2\sqrt{\beta}}\right)\right\} \\ &+ \frac{\alpha}{\sqrt{\beta}} D\left(\sqrt{\beta}(t-\gamma^{-1}) + \frac{\alpha}{2\sqrt{\beta}}\right), \end{aligned} \quad [14]$$

for convenience of notation, and $D(x)$ is Dawson's function.(57)

Equation (13) joins three continuously differentiable solutions, the initial plateau phase, the initial decay phase, and the exponential decay phase. The solution was fit to the fluorescence data using least squares fitting in Matlab(58). The fitted solutions are superimposed on the experimental data in Fig. 7c, and show very good agreement. The list of fitted parameters is given in Table S4.

Monomer	Residue name	Residue ID	Atom name	Monomer	Residue name	Residue ID	Atom name
EMR1	GLU	14	OE1	EMR1	GLU	14	OE2
EMR1	TYR	40	CD2	EMR1	TYR	40	CE2
EMR1	SER	43	CB	EMR1	SER	43	OG
EMR1	SER	43	C	EMR1	SER	43	O
EMR1	LEU	47	CD2	EMR1	TRP	63	CD1
EMR1	TRP	63	NE1	EMR1	TRP	63	CE2
EMR1	TRP	63	CZ3	EMR1	TRP	63	CZ2
EMR1	TRP	63	CH2	EMR2	GLU	14	CB
EMR2	GLU	14	CG	EMR2	GLU	14	CD
EMR2	GLU	14	OE1	EMR2	GLU	14	OE2
EMR2	THR	18	CB	EMR2	THR	18	OG1
EMR2	THR	18	CG2	EMR2	TYR	40	CA
EMR2	TYR	40	CB	EMR2	TYR	40	CG
EMR2	TYR	40	CE1	EMR2	TYR	40	CZ
EMR2	TYR	40	OH	EMR2	TYR	40	CD2
EMR2	TYR	40	CE2	EMR2	TYR	40	C
EMR2	TYR	40	O	EMR2	SER	43	CA
EMR2	SER	43	CB	EMR2	SER	43	OG
EMR2	SER	43	C	EMR2	SER	43	O
EMR2	PHE	44	N	EMR2	PHE	44	CA
EMR2	PHE	44	CG	EMR2	PHE	44	CD1
EMR2	PHE	44	CE1	EMR2	PHE	44	CZ
EMR2	PHE	44	CD2	EMR2	PHE	44	CE2
EMR2	LEU	47	CD2	EMR2	TYR	60	CE1
EMR2	TYR	60	CZ	EMR2	TYR	60	OH
EMR2	TYR	60	CD2	EMR2	TYR	60	CE2
EMR2	TRP	63	CB	EMR2	TRP	63	CG
EMR2	TRP	63	CD1	EMR2	TRP	63	NE1
EMR2	TRP	63	CE2	EMR2	TRP	63	CD2
EMR2	TRP	63	CZ2	EMR2	TRP	63	CH2

Table S3. Orientation atoms used to define the RMSD restraint to confine TPP to the active site of $EmrE$. The atoms are shown in Fig. 12 of the main text. The atom naming convention is taken from the CHARMM36 force field.(34)

Peptide	t_0(s)	γ(s^{-1})	k_{EmrE}	k_{diff}
No peptide	329.7 $\pm$ 12.4	0.002342 $\pm$ 0.0002	0.00247 $\pm$ 0.0001	0.001 $\pm$ 0.0001
A87-I94	239.3 $\pm$ 25.3	0.002352 $\pm$ 0.0004	0.00103 $\pm$ 0.0001	0.002 $\pm$ 0.0002
I88-C95	330.1 $\pm$ 14.3	0.001855 $\pm$ 0.0002	0.00266 $\pm$ 0.0002	0.001 $\pm$ 0.0001
I89-A96	310.1 $\pm$ 15.9	0.002097 $\pm$ 0.0002	0.00198 $\pm$ 0.0002	0.001 $\pm$ 0.0001
M92-L99	467.7 $\pm$ 55.6	0.003157 $\pm$ 0.0014	0.00060 $\pm$ 0.0001	0.002 $\pm$ 0.0003

Table S4. Model parameters for Eq. (11) fit from fluorescence data with 95% confidence limits. Experimental fluorescence curves and models fits are shown in Fig. 7 of the main text.

References

1. Gutman N, Steiner-Mordoch S, Schuldiner S (2003) an Amino Acid Cluster Around the Essential Glu-14 Is Part of the Substrate and Proton Binding Domain of EmrE, a Multidrug Transporter from Escherichia Coli. *J Biol Chem* 278:16082–16087.
2. Schuldiner S (2009) EmrE, a Model for Studying Evolution and Mechanism of Ion-Coupled Transporters. *Biochim Biophys Acta* 1794(5):748–62.
3. Brooks B, et al. (2009) CHARMM: The Biomolecular Simulation Program. *J Comput Chem* 30:1545–1614. PMC2810661.
4. Bateman A, et al. (2004) The Pfam Protein Families Database. *Nucleic acids research* 32:D138–41.
5. Lloris-Garcerá P, et al. (2013) In Vivo Trp Scanning of the Small Multidrug Resistance Protein EmrE Confirms 3D Structure Models. *J Mol Biol* 425(22):4642–51.
6. Amadi ST, Koteiche Ha, Mishra S, McHaourab HS (2010) Structure, Dynamics, and Substrate-Induced Conformational Changes of the Multidrug Transporter EmrE in Liposomes. *J Biol Chem* 285(34):26710–8.
7. Henzler-Wildman K (2012) Analyzing Conformational Changes in the Transport Cycle of EmrE. *Curr Opin Stuc Biol* 28:38–43.
8. Banigan J, Gayen A, Cho M, Traaseth N (2015) A Structured Loop Modulates Coupling Between the Substrate-Binding and Dimerization Domains in the Multidrug Resistance Transporter EmrE. *J Biol Chem* 290(2):805–14.
9. Eswar N, et al. (2006) Comparative Protein Structure Modeling Using Modeller. *Curr Prot Bioinf* Chapter 5:Unit 56.
10. Elbaz Y, Salomon T, Schuldiner S (2008) Identification of a Glycine Motif Required for Packing in EmrE, a Multidrug Transporter from Escherichia Coli. *J Biol Chem* 283:12276–12283.
11. Poulsen B, Rath A, Deber C (2009) The Assembly Motif of a Bacterial Small Multidrug Resistance Protein. *J Biol Chem* 284 (15):9870–5.
12. Soskine M, Adam Y, Schuldiner S (2004) Direct Evidence for Substrate Induced Proton Release in Detergent Solubilized EmrE, a Multidrug Transporter. *J Biol Chem* 279:9951–9955.
13. Adam Y, Tayer N, Rotem D, Schreiber G, Schuldiner S (2007) the Fast Release of Sticky Protons: Kinetics of Substrate Binding and Proton Release in a Multidrug Transporter. *Proc Natl Acad Sci U S A* 104:17989–17994.
14. Morrison E, Robinson A, Liu Y, Henzler-Wildman K (2015) Asymmetric Protonation of EmrE. *J Gen Physiol* 146(6):445–61.
15. McIntosh L, et al. (2011) Dissecting Electrostatic Interactions in Bacillus Circulans Xylanase Through NMR-Monitored PH Titrations. *J Biomol NMR* 51(1-2):5–19.
16. Chen YJ, et al. (2007) X-Ray Structure of EmrE Supports Dual Topology Model. *Proc Natl Acad Sci U S A* 104(48):18999–9004.
17. Brooks B, et al. (1983) CHARMM: A Program for Macromolecular Energy, minimization, and dynamics calculations. *J Comput Chem* 4:187–217.
18. Krivov GG, Shapovalov MV, Dunbrack Jr RL (2009) Improved Prediction of Protein Side-Chain Conformations with SCWRL4. *Proteins* 77:778–795.
19. Lu B, Zhou Y, Holst M, McCammon J (2008) Recent Progress in Numerical Methods for the Poisson-Boltzmann Equation in Biophysical Applications. *Commun Comput Physics* 3:973–1009.
20. Koehl P, Delarue M (1994) Application of a Self-Consistent Mean Field Theory to Predict Protein Side-Chains Conformation and Estimate Their Conformational Entropy. *J Mol Biol* 239:249–275.
21. Lazaridis T (2003) Effective Energy Function for Proteins in Lipid Membranes. *PROTEINS: Struct Func Genet* 52(2):176–192.
22. Vanommeslaeghe K, et al. (2009) CHARMM General Force Field: A Force Field and Drug-like Molecules Compatible with the CHARMM All-Atom Additive Biological Force Fields. *J Comput Chem* 31:671–690.
23. MacKerell Jr A, Feig M, Brooks III C (2004) Extending the treatment of backbone energetics in protein force fields: Limitations of gas-phase quantum mechanics in reproducing protein conformational distributions in molecular dynamics simulations. *J Comput Chem* 25:1400–1415.
24. Mayne CG, Saam J, Schulten K, Tajkhorshid E, Gumbart JC (2013) Rapid Parameterization of Small Molecules Using the Force Field Toolkit. *Journal of Computational Chemistry* 34(32):2757–2770.
25. Ovchinnikov V. EmrE MD Simulation Coordinates and Simulation Parameters. Mendeley Data, v2 (2018). URL http://dx.doi.org/10.17632/3pvz4hytfd.2.
26. Jo S, Lim J, Klauda J, Im W (2009) CHARMM-GUI Membrane Builder for Mixed Bilayers and Its Application to Yeast Membranes. *Biophys J* 97:50–58.
27. Harvey M, Giupponi G, Fabritiis GD (2009) ACEMD: Accelerated Molecular Dynamics Simulations in the Microseconds Timescale. *J Chem Theory and Comput* 5:1632–1639.
28. Morrison EA, et al. (2012) Antiparallel EmrE Exports Drugs by Exchanging Between Asymmetric Structures. *Nature* 481:45–52.
29. Wu X, Subramaniam S, Case D, Wu K, Brooks B (2013) Targeted Conformational Search with Map-Restrained Self-Guided Langevin Dynamics: Application to Flexible Fitting into Electron Microscopic Density Maps. *J Struc Biol* 183(3):429–40.
30. Klauda JB, et al. (2010) Update of the CHARMM All-Atom Additive Force Field for Lipids: Validation on Six Lipid Types. *J Phys Chem B* 114:7830–7843.
31. Rath A, Melnyk RA, Deber CM (2006) Evidence for Assembly of Small Multidrug Resistance Proteins by a "Two-Faced" Transmembrane Helix. *J Biol Chem* 281:15546–15553.
32. Verdine GL, Hilinski GJ (2012) *Stapled Peptides for Intracellular Drug Targets*. (Elsevier Inc) Vol. 503, 1 edition, pages 3–33.
33. Baek S, et al. (2012) Structure of the Stapled P53 Peptide Bound to Mdm2. *J Am Chem Soc* 134(1):103–6.
34. Best R, et al. (2012) Optimization of the Additive CHARMM All-Atom Protein Force Field Targeting Improved Sampling of the Backbone ϕ, ψ and Side-Chain χ_1 and χ_2 Dihedral Angles. *J Chem Theor Comput* 8:3257–3273.
35. Guvench O, et al. (2011) CHARMM Additive All-Atom Force Field for Carbohydrate Derivatives and Its Utility in Polysaccharide and Carbohydrate-Protein Modeling. *J Chem Theor Comput* 7(10):3162–3180.

36. Phillips J, et al. (2005) Scalable Molecular Dynamics with NAMD. *J Comput Chem* 26:1781–1802.
37. Liu P, Dehez F, Cai W, Chipot C (2012) A Toolkit for the Analysis of Free-Energy Perturbation Calculations. *Journal of Chemical Theory and Computation* 8(8):2606–2616.
38. de Ruiter A, Boresch S, Oostenbrink C (2013) Comparison of Thermodynamic Integration and Bennett Acceptance Ratio for Calculating Relative Protein-Ligand Binding Free Energies. *J Comput Chem* 34(12):1024–34.
39. Boresch S, Tettinger F, Leitgeb M, Karplus M (2003) Absolute Binding Free Energies: A Quantitative Approach for Their Calculation. *The Journal of Physical Chemistry B* 107(35):9535–9551.
40. Gumbart J, Roux B, Chipot C (2013) Standard Binding Free Energies from Computer Simulations: What Is the Best Strategy? *J Chem Theor Comput* 9(1):794–802.
41. Hermans J, Wang L (1997) Inclusion of Loss of Translational and Rotational Freedom in Theoretical Estimates of Free Energies of Binding. *J Am Chem Soc* 119:2707–2714.
42. Tyka M, Clarke A, Sessions R (2006) An Efficient, path-independent method for free-energy calculations. *J Phys Chem B* 110: 17212–17220.
43. Ovchinnikov V, Karplus M (2012) Analysis and elimination of a bias in targeted molecular dynamics simulations of conformational transitions: Application to Calmodulin. *J Phys Chem B* 116:8584–8603. PMC3406239.
44. Kabsch W (1976) A Solution for the Best Rotation to Relate Two Sets of Vectors. *Acta Cryst* A32:922–923.
45. Ovchinnikov V, Nam K, Karplus M (2016) a Simple and Accurate Method to Calculate Free Energy Profiles and Reaction Rates from Restrained Molecular Simulations of Diffusive Processes. *J Phys Chem B* 120:8457–8472.
46. Ovchinnikov V, Karplus M, Vanden-Eijnden E (2011) Free Energy of Conformational Transition Paths in Biomolecules: The String Method and Its Application to Myosin VI. *J Chem Phys* 134:085103. PMC3060930.
47. Ovchinnikov V, Cecchini M, Vanden-Eijnden E, Karplus M (2011) A Conformational Transition in the Myosin VI Converter Contributes to the Variable Step Size. *Biophys J* 101:2436–2444. PMC3218336.
48. Hill TL (1986) *An Introduction to Statistical Thermodynamics.* (Dover, New York).
49. Baker N, Sept D, Joseph S, Holst M, McCammon J (2001) Electrostatics of Nanosystems: Application to Microtubules and the Ribosome. *Proc Natl Acad Sci USA* 98:10037–10041.
50. Platzer G, Okon M, McIntosh L (2014) pH-Dependent Random Coil (1)H, (13)C, and (15)N Chemical Shifts of the Ionizable Amino Acids: A Guide for Protein PK a Measurements. *J Biomol NMR* 60(2-3):109–29.
51. Callenberg K, Choudhary O, de Forest G, Gohara D, Baker N (2010) APBSmem: A Graphical Interface for Electrostatic Calculations at the Membrane. *PLoS ONE* 5:e12722.
52. Cohen B, et al. (2002) Probing Protein Electrostatics with a Synthetic Fluorescent Amino Acid. *Science* 296:1700–1703.
53. Gilson M, Honig B (2004) Calculation of the Total Electrostatic Energy of a Macromolecular System: Solvation Energies, binding energies, and conformational analysis. *Proteins: Struct Funct Bioinf* 4:7–18.
54. Bellmann-Sickert K, Stone T, Poulsen B, Deber C (2015) Efflux by Small Multidrug Resistance Proteins Is Inhibited by Membrane-Interactive Helix-Stapled Peptides. *J Biol Chem* 290(3):1752–9.
55. Tal N, Schuldiner S (2009) A Coordinated Network of Transporters with Overlapping Specificities Provides a Robust Survival Strategy. *Proc Natl Acad Sci USA* 9051-9056:106.
56. Poulsen BE, Deber CM (2012) Drug Efflux by a Small Multidrug Resistance Protein Is Inhibited by a Transmembrane Peptide. *Antimicrob Agents Chemother* 56:3911–3916.
57. Abramowitz M, Stegun I (1970) *Handbook of Mathematical Functions.* (Dover Publications Inc, New York).
58. MATLAB (2010) *Version 7100 (R2010a).* (The MathWorks Inc, Natick, Massachusetts).